

A New Stereo Benchmarking Dataset for Satellite Images

Sonali Patil

Bharath Comandur

Tanmay Prakash

Avinash C. Kak

School of Electrical and Computer Engineering, Purdue University
West Lafayette, IN, USA

patil19@purdue.edu

bcomandu@purdue.edu

tprakash@purdue.edu

kak@purdue.edu

Abstract

In order to facilitate further research in stereo reconstruction with multi-date satellite images, the goal of this paper is to provide a set of stereo-rectified images and the associated groundtruthed disparities for 10 AOIs (Area of Interest) drawn from two sources: 8 AOIs from IARPA's MVS Challenge dataset and 2 AOIs from the CORE3D-Public dataset. The disparities were groundtruthed by first constructing a fused DSM from the stereo pairs and by aligning 30 cm LiDAR with the fused DSM. Unlike the existing benchmarking datasets, we have also carried out a quantitative evaluation of our groundtruthed disparities using human annotated points in two of the AOIs. Additionally, the rectification accuracy in our dataset is comparable to the same in the existing state-of-the-art stereo datasets. In general, we have used the WorldView-3 (WV3) images for the dataset, the exception being the UCSD area for which we have used both WV3 and WorldView-2 (WV2) images. All of the dataset images are now in the public domain. Since multi-date satellite images frequently include images acquired in different seasons (which creates challenges in finding corresponding pairs of pixels for stereo), our dataset also includes for each image a building mask over which the disparities estimated by stereo should prove reliable. Additional metadata included in the dataset includes information about each image's acquisition date and time, the azimuth and elevation angles of the camera, and the intersection angles for the two views in a stereo pair. Also included in the dataset are both quantitative and qualitative analyses of the accuracy of the groundtruthed disparity maps. Our dataset is available for download at <https://engineering.purdue.edu/RVL/Database/SatStereo/index.html>

1. Introduction

While there now exist several datasets for projective cameras that can be used to test the performance of stereo matching algorithms, the same cannot be said for the push-

broom cameras used for satellite images. The images produced by the pushbroom cameras are particularly challenging for stereo disparity calculations because their epipolar lines (which in reality are curves) do not form conjugate pairs. Additional sources of difficulty are the facts that the images are generally recorded at different times and during different seasons, which creates difficulties in establishing matches between the corresponding pixels in the images of a stereo pair.

The goal of this paper is to remedy this shortcoming in the research community by providing a dataset with groundtruthed disparities for: (1) eight AOIs (Area of Interests) in San Fernando, Argentina, as defined in the IARPA's MVS Challenge dataset [7]. That challenge dataset, spanning 100 square kilometers, includes 30 cm airborne LiDAR groundtruth data for a 20 square kilometer subset of the larger area. All this data is now publicly available and we have utilized it for constructing our groundtruthed disparity maps. And (2) two AOIs from the CORE3D-Public dataset [8] covering areas in UCSD and Jacksonville. In general, we have drawn stereo pairs from WV3. The exception is the UCSD area, for which we have used both WV2 and WV3 images. The AOIs included in the dataset vary in size from 0.1 sq. km. to 2 sq. km. and the number of selected stereo pairs for the different AOIs varies from 53 to 505. One of the major challenges presented by out-of-date satellite imagery is that some of the scene content may vary from image to image. Figure 2 illustrates how in the MVS MasterProvisional 2 area variations in scene content are more prominent in ground regions as compared to building regions. Therefore, we provide building masks to mark regions where we can expect relatively high accuracies for the groundtruthed disparities. This is not to imply that the groundtruthed disparities for the ground regions are always unreliable.

In order to facilitate research in large-scale stereo reconstruction, we also provide additional metadata for each stereo pair, which includes the information about each image's acquisition date and time, the azimuth and elevation angles for the images, and the intersection angle of the two

$\tau = 140$ days, $\theta = 32.28^\circ$ $\tau = 162$ days, $\theta = 33.86^\circ$ $\tau = 43$ days, $\theta = 23.25^\circ$ $\tau = 18$ days, $\theta = 15.30^\circ$

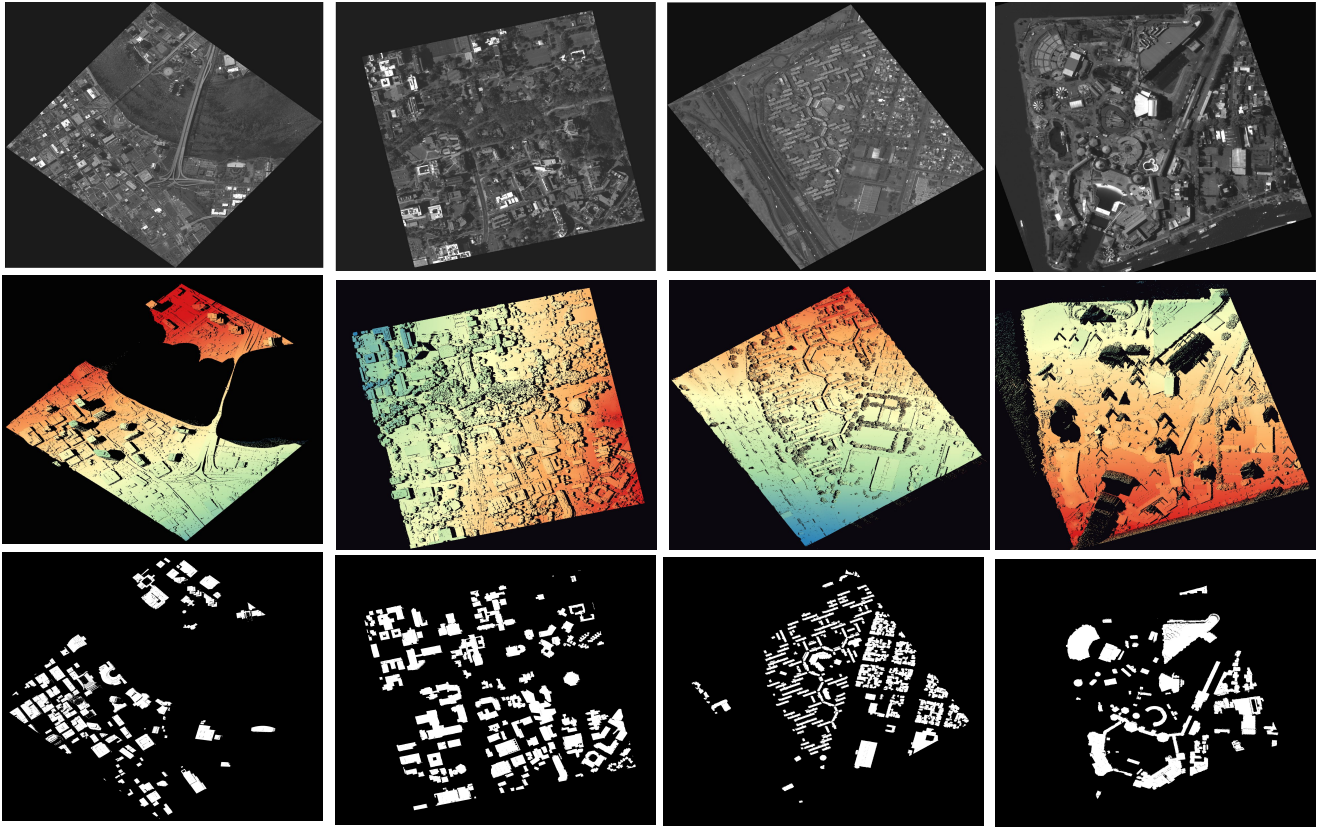


Figure 1: Qualitative results for our groundtruthed disparity maps from the top four largest AOIs. From left to right the AOIs are: Jacksonville, UCSD WV2, Explorer, and MasterSequestered (MS) Park. For additional results, please see the supplemental material submitted with this manuscript. Note that the large holes in MS Park are either in the water regions or the surrounding land regions. Since the LiDAR output is sensitive to specularly reflective surfaces, the heights as provided by LiDAR in such regions are either invalid values or large noise spikes. τ and θ represent the time difference between a stereo pair and the intersection angle, respectively.

views. Such metadata can help to see a correlation between these parameters and stereo matching quality.

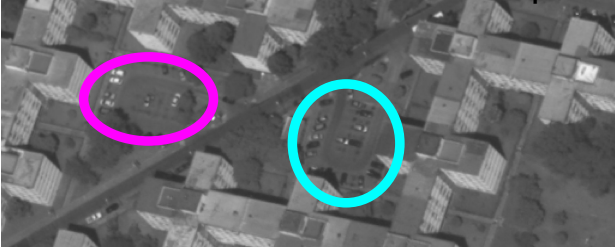
A unique aspect of our dataset is that we have carried out a quantitative evaluation of our groundtruthed disparities using human annotated points in two AOIs. Additionally, we have evaluated the stereo rectification accuracies; the rectification errors are less than 0.5 pixels on the average.

The dataset itself consists of a set of selected stereo-rectified image pairs for each of the ten AOIs and presents the groundtruthed disparities for each pixel in a reference image and the corresponding secondary image in each pair. The stereo pair selection is based on time difference and view-angle difference considerations. For each AOI, the disparities are groundtruthed by first constructing a fused DSM (Digital Surface Model) from the stereo pairs and,

subsequently, by aligning the LiDAR with the fused DSM. This process of aligning LiDAR with the fused DSM allows for a mapping from each pixel (x,y) in the reference rectified image of a stereo pair to what the true value of the disparity should be at that pixel. The process of extracting the groundtruthed disparities at the different pixels in a reference stereo-rectified image involves back projecting pixels of the rectified image and using the lat/long coordinates thus calculated to get the corresponding height from the LiDAR data. Subsequently, this height value is translated into the disparity value. Also included in the dataset are both quantitative and qualitative analyses of the accuracy of the groundtruthed disparity maps.

Table 1 presents the summary of our dataset. Figure 1 shows some examples of our disparity maps from the top four largest AOIs, along with their corresponding building

Stereo Rectified Reference Chip



Stereo Rectified Secondary Chip



Figure 2: A stereo rectified chip pair from the MP2 AOI, with the images acquired roughly six months apart. This example illustrates significant variations in the ground-level scene content. The highlighted ground-level regions show changes in the parking lots due to changes in the number of cars and the changes in the shadows.

masks and metadata.

Dataset	WV3 / WV2	Area (sq. km.)	No. of Selected Stereo Pairs
MP 1 (MVS)	WV3	0.13	505
MP 2 (MVS)	WV3	0.14	361
MP 3 (MVS)	WV3	0.10	246
Explorer (MVS)	WV3	0.45	329
MS 1 (MVS)	WV3	0.12	501
MS 2 (MVS)	WV3	0.13	499
MS 3 (MVS)	WV3	0.12	349
MS Park (MVS)	WV3	0.25	301
UCSD (CORE3D)	WV2	1	336
UCSD (CORE3D)	WV3	1	130
Jax (CORE3D)	WV3	2	53

Table 1: MVS stands for IARPA’s Multi-View Stereo Challenge, MP stands for MasterProvisional and MS stands for MasterSequestered

The rest of the paper is organized as follows: Section 2 briefly outlines the related work. In Section 3 we explain how we use the notions of “chips” and “tiles” as used in

groundtruthing the disparity maps. We take up image-to-image and LiDAR-to-fused DSM alignment issues in Section 4. Section 5 shows how aligned LiDAR is used to calculate the groundtruth disparities. In Section 6 we present a quantitative evaluation of the groundtruth disparity maps and some benchmarking results of existing stereo matching algorithms. Finally in Section 7 we conclude our findings.

2. Related Work

3D reconstruction is a popular area of research in the computer vision community and there exist a number of groundtruthed datasets for benchmarking stereo matching algorithms. Although synthetic datasets created using rendered scenes such as the MPI Sintel stereo dataset [10] might prove useful for certain tasks, they do not necessarily capture the diversity and complexity of images of the real world. Since our dataset has been created to serve as a benchmark for binocular stereo, it is sufficient to restrict our discussion of related work to datasets that focus on binocular stereo. The well known Tsukuba image pair [21] was one of the first stereo datasets and contains disparity maps created using manual annotation. Since then, multiple attempts have been made to create more accurate datasets and some of the most popular ones include the Middlebury, KITTI and ETH3D datasets.

The Middlebury datasets include the Middlebury2001 [25], Middlebury2003 [26], Middlebury2005 and Middlebury2006 datasets [17] and more recently the high resolution Middlebury 2014 dataset [24]. The last dataset was created using a stereo rig with cameras and structured light projectors and claims subpixel-accurate groundtruth. Images are of resolution (5-6MP) and mostly contain indoor scenes. Pairs are grouped under different categories such as similar and varying ambient illumination, perfect and imperfect rectification etc. Note that less than 50% of the scenes required manual cleanup [24].

With a focus on autonomous driving, the KITTI2012 [13] and KITTI2015 [20] datasets were created to capture outdoor scenes. While the former pays attention to static environments, the latter is concerned with moving objects captured by a stereo camera. For generating groundtruth, scans were captured using a laser scanner mounted on a car and scenes were annotated using 3D CAD models for moving vehicles. The disparity maps in this dataset are semi-dense when compared to the Middlebury2014 dataset.

The ETH3D [27] dataset was created to address some of the shortcomings of the the above mentioned datasets including small size, lower diversity, absence of outdoor scenes (Middlebury), low resolution and sparseness (KITTI). Groundtruth depth was captured using a high precision laser scanner. It covers both indoor and outdoor scenes and can be used to evaluate both binocular and multi-view stereo algorithms.

The datasets described thus far consist of images taken with projective cameras that are either handheld or mounted on stereo rigs. Recently, there was an announcement of a stereo dataset for satellite images [6] that also provides groundtruthed disparities. That dataset however does not provide estimates of the errors in the groundtruthed disparities using human annotated points. Additionally, that dataset also does not present any information on the rectification errors involved. Note also that the framework we have used for creating the dataset is significantly different from the one used in [6]. We believe that the research community can only benefit by experimenting with datasets produced with two different approaches.

3. Chip versus Tile Conundrum

Each of the AOIs in our dataset is specified by a KML polygon in the lat/long space. The portions of the satellite images extracted through each of these polygons are referred to as *chips*. Chips come in varying sizes, depending on the size of the AOI. The largest of the chips are of size roughly 5000×5000 . Our goal is to provide groundtruthed disparities at the chip level so that a disparity map would cover the entire AOI.

Unfortunately, on account of the fact that, in general, the pushbroom cameras used in the satellites are characterized by non-conjugate epipolar curves, it is possible for the chip pairs to be much too large for a straightforward implementation of stereo rectification. There do exist two different approaches to get around this difficulty: (1) To use the approach suggested by Oh et. al. [22] that consists of first finding piecewise correspondences between the different possible epipolar curve pairs and then resampling the original images in a way that straightens out the epipolar curves. And (2) To use the method proposed by Franchis et al [11] that consists of breaking the chips into smaller tiles under the assumption that the part of the epipolar curve spanning a tile may be well approximated by a straight line. Another way of saying the same thing would be that the image portions in the tiles may be considered to have come from an affine imaging sensor. Following [11], we have used the latter approach. The tiles that we use are typically of size 500×500 .

That then takes us to the heart of the algorithmic problem we needed to solve for generating the groundtruthed dataset: How to jump from the initial stereo rectifications based on tile based processing to the final stereo rectifications for the chips that would be needed for the dataset? While the initial stereo rectification would be applied to the *tiles* that would typically be of size 500×500 , we would want to translate that into the final stereo rectifications of the *chips* that may be as large as 5000×5000 for the larger AOIs.

As to how we solve this chip vs. tile conundrum is best

explained through the overall processing architecture we employ as shown in Fig. 3.

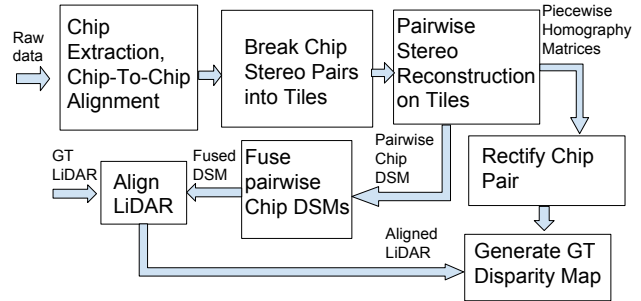


Figure 3: Overall pipeline of our approach, showing difference between chip-level processing and tile-level processing

As shown in the figure, the raw satellite images are first subject to KML-based chip extraction for the AOIs. All the chips thus collected for each AOI are subject to pair selection (not shown) followed by chip-to-chip alignment and RPC bias correction as described in Section 4 and its subsections. As shown in the middle box in the upper row, each chip is subsequently broken into tiles; for this we use the s2p logic directly [11]. Breaking the chips into tiles allows for conventional stereo rectification between pairs of tiles, and that, in turn, allows for relatively easy stereo reconstruction from the tiles. The tile-based stereo reconstructions serve two purposes: (1) On a pairwise basis, they yield the point clouds that when aggregated together give us the chip-based pairwise DSMs as explained in Section 4.5. In Fig. 3, this is represented by the downward pointing arrow that emanates from the box labeled “Pairwise Stereo Rectification on Tiles”. And (2), the homographies that describe tile-based rectifications when modified by tile locations inside the chips give us the chip-based rectifications as explained in Section 4.4.2. The rest of Fig. 3 should be self explanatory.

4. Data Alignment

There are two types of data alignment carried out in the processing architecture shown in Fig. 3: chip-to-chip alignment and the LiDAR-to-fused-DSM alignment. Both of these are captured by the pipeline shown in Figure 4.

Note that the LiDAR-to-fused-DSM alignment is at the chip level of processing. Of the various steps shown in the figure, we will cover chip extraction and radiometric correction details in Section 4.1 that is devoted to the preprocessing of the raw images. That will be followed in Section 4.2 by how the RPC bias errors are estimated and the RPCs corrected. Section 4.3 describes the logic we have

used for pair selection; this logic is based on a combination of the difference in the image acquisition times and the difference between the view-angles. The other steps shown in the pipeline are covered in Sections 4.4 and 4.5 .

4.1. Preprocessing

It is important to apply Top-of-Atmosphere correction when using multi-date images. This involves the following steps – 1) converting the pixel values into ToA spectral radiance i.e. the spectral radiance entering the telescope aperture and subsequently 2) converting the ToA radiance to ToA reflectance values, which effectively converts the earth-sun distance to 1 Astronomical Unit (AU) and the solar zenith angle to 0 degrees. Further details about the ToA correction for WV2 and WV3 images can be found in [2] and [3], respectively.

4.2. RPC Correction

According to [14], good alignment between satellite images can be achieved by adding a constant bias to the pixel locations output by the RPC model, rather than explicitly updating the physical geometry of the camera. We therefore correct the RPC model by jointly calculating the appropriate biases for each RPC, using the popular approach of bundle adjustment [4].

Bundle adjustment aligns the images by jointly optimizing 3D structure and the camera parameters over a global objective function. First, we detect tie point correspondences between images. Corresponding tie points are image points that have been identified as the projections of the same 3D world points. The reprojection error of a tie point is the distance between a projection of an estimated world point and the tie point. It is a function of both the camera parameters and the world point. By jointly finding the world point coordinates and camera parameters that minimize the total reprojection error over the full set of tie point correspondences, we can align the images.

To populate the set of tie point correspondences, we compare every possible pair of images. Given a pair of images, we extract interest points in each image using SURF [5], identify an initial set of tie point correspondences between the two images using the SURF feature descriptor, and prune outliers from that set of correspondences using RANSAC.

4.3. Stereo Pair Selection

Not all pairs — especially so in the context of satellite stereo reconstruction — are equal. Intuitively it makes sense that disparity calculations would be aided by similar scene content between images. Although designing a theoretically correct way to select image pairs is a difficult task, it is possible to use heuristics to improve the chances of selecting good pairs. Along the lines of the pair selection

strategy used in [12], we first apply thresholds to the view angles to drop the highly off-nadir and the highly near-nadir images. We then select the pairs by applying thresholds to the differences in the view angles and the differences in times of acquisition between the images in each pair. The pairs thus chosen are subsequently sorted in increasing order of the time differences involved, the intuition being that images captured closer in time have a greater probability of having similar scene content. Note that the WV2 and WV3 sensors are heliosynchronous, i.e. they image the same location on the earth’s surface at roughly the same time every day.

4.4. Stereo Rectification

In this section we will go over the details of chip rectification. First, we will cover the details of tile-based rectification in Section 4.4.1. Then, in Section 4.4.2 we will cover the details of how we use the output from the tile-based rectification step to stereo rectify the full chips.

4.4.1 Stereo Rectification — Tile Based

For stereo rectifying tiles, we have used the approach proposed by [11]. We first approximate an RPC projection function into an affine projection with first order Taylor series approximation. Let $\mathcal{P}_{RPC} : \mathbb{R}^3 \rightarrow \mathbb{R}^2$ be the RPC projection function. The first order Taylor series expansion of \mathcal{P}_{RPC} around a 3D world point \mathbf{X}_o can be given as

$$\begin{aligned} \mathcal{P}_{RPC}(\mathbf{X}) &= \mathcal{P}_{RPC}(\mathbf{X}_o) + \nabla \mathcal{P}_{RPC}(\mathbf{X}_o)(\mathbf{X} - \mathbf{X}_o) \\ &= \nabla \mathcal{P}_{RPC}(\mathbf{X}_o)\mathbf{X} + \mathbf{b} \end{aligned}$$

where $\mathbf{b} = \mathcal{P}_{RPC}(\mathbf{X}_o) - \nabla \mathcal{P}_{RPC}(\mathbf{X}_o)\mathbf{X}_o$ and $\nabla \mathcal{P}_{RPC}(\cdot)$ is the Jacobian matrix. The affine approximation of $\mathcal{P}_{RPC}(\cdot)$ can be expressed as a 3×4 matrix in homogeneous coordinates as follows

$$\mathcal{P}_{Affine}(\mathbf{X}) = \begin{bmatrix} \nabla \mathcal{P}_{RPC}(\mathbf{X}_o) & \mathbf{b} \\ 0 & 1 \end{bmatrix}^{3 \times 4} \begin{bmatrix} \mathbf{X} \\ 1 \end{bmatrix}^{4 \times 1}$$

After this step, we can apply off-the-shelf algorithms for stereo rectifying each pair. For the sake of completeness we will summarize those steps here. First, we find the correspondences $\mathbf{x}_j \leftrightarrow \mathbf{x}'_j$ using SIFT matches ([19], [23]), where \mathbf{x}_j is a point in a reference view and \mathbf{x}'_j is the corresponding point in the secondary view. Then we estimate the fundamental matrix F [15] with RANSAC, using $\mathbf{x}'_j{}^T F \mathbf{x}_j = 0$. Finally we estimate resampling homographies H and H' from F [18] by solving the following equation

$$F = H'^T \begin{bmatrix} 0 & 0 & 0 \\ 0 & 0 & -1 \\ 0 & 1 & 0 \end{bmatrix} H$$

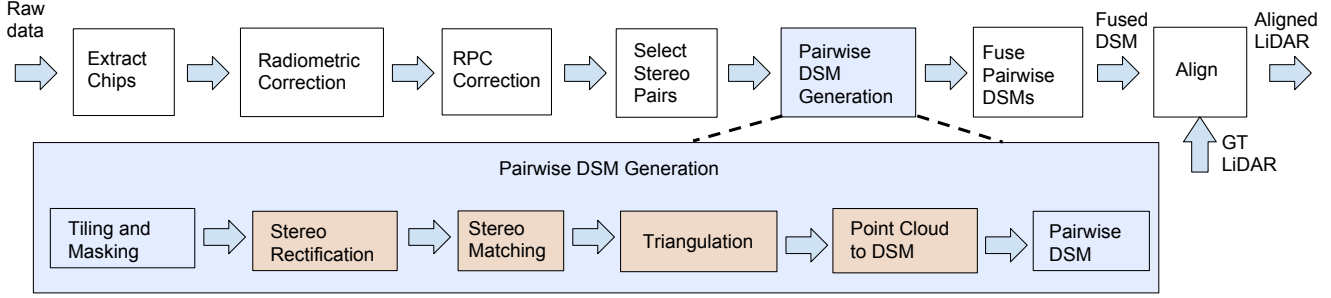


Figure 4: The input raw data includes RPC files for camera parameters and NTF files for raw sensor data. SRTM (Shuttle Radar Tomography Mission) DEM (Digital Elevation Model) and KML vector which is, used to extract AOIs. The steps in orange color are processed in parallel per tile.

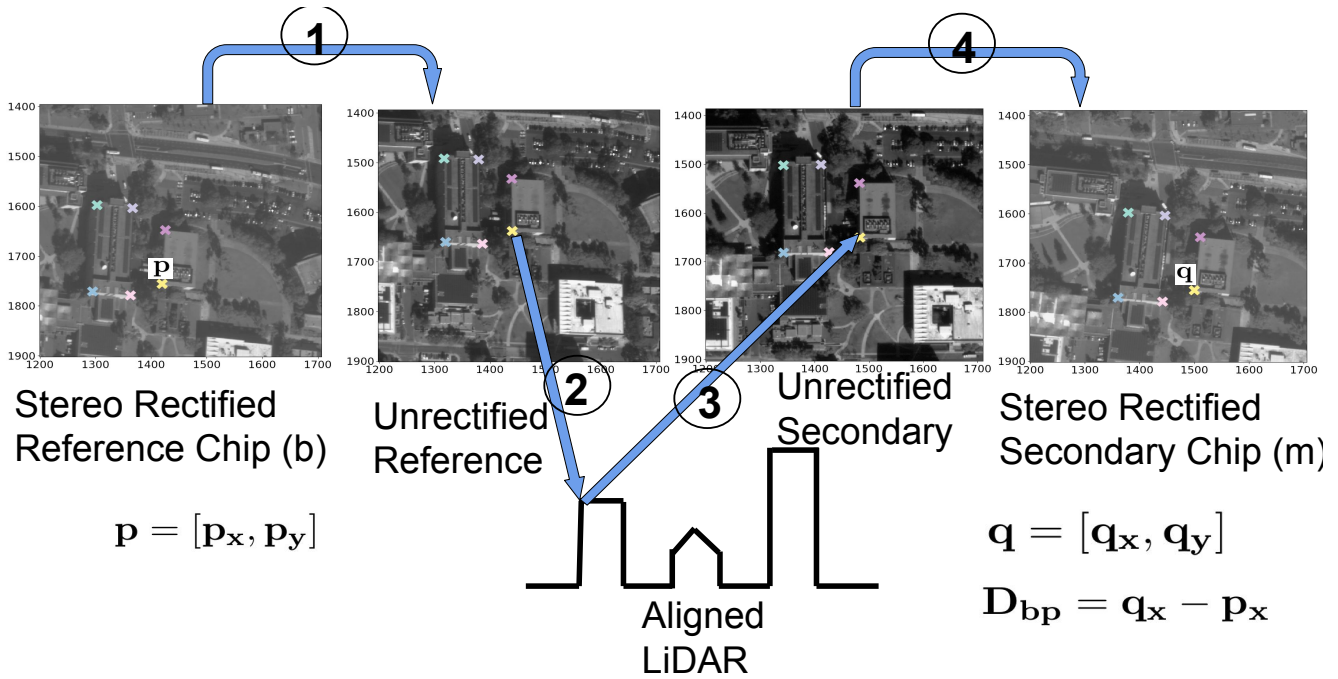


Figure 5: Overview of our groundtruthing process. Referring to labels 1-4 in the figure, (1) We map points from stereo rectified reference view to unrectified reference view (2) we backproject these point into aligned LiDAR using inverse RPC, giving us latitude, longitude and height for each point (3) we forward project these world points onto secondary unrectified view (4) Using inverse rectification map we map these points into stereo rectified secondary view. After performing steps 1 through 4, we can now apply the definition of disparity to get disparity value at each point.

For stereo reconstruction, these homographies are further modified by apply required translation so that the tiles origin is moved to (0,0). We store both H and H' before applying translation for stereo rectifying full chips as explained in the next section 4.4.2.

4.4.2 Stereo Rectification — Chip Based

Given two images l and r , and a point p_1 in image l then we can define the parametric equation for the epipolar curve as follows:

$$epi_{lr}^{p_1}(h) = \mathcal{P}_{RPC_r}(\mathcal{P}_{RPC_l}^{-1}(p_x, p_y, h))$$

Intuitively, it contains the locations for all possible correspondences in the secondary image for a given point p_1 in the reference image for different height values for h . For a

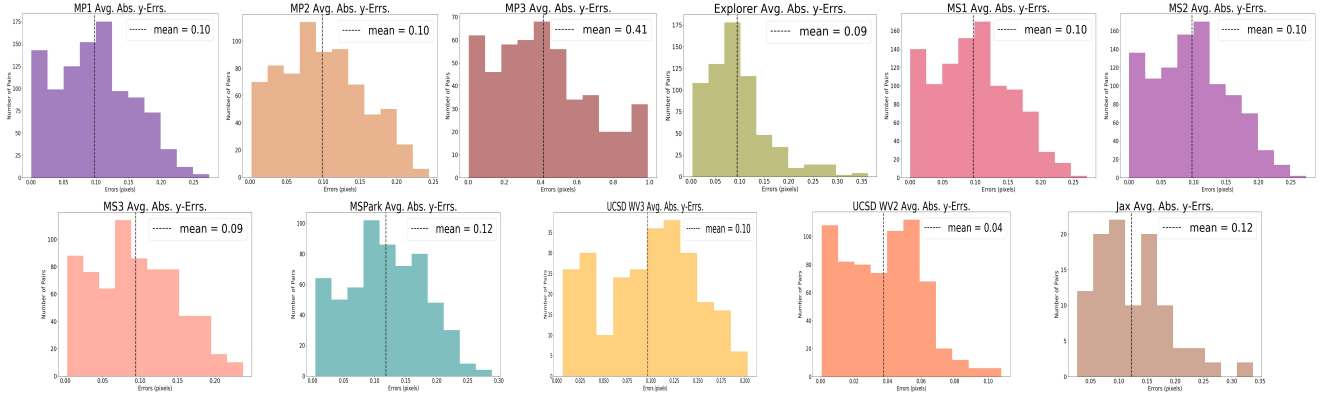


Figure 6: Average chip-level rectification error (absolute y-error) distributions for all eleven datasets.

pinhole camera, epipolar lines form conjugate pairs. However, this property does not hold true for the epipolar curves for the pushbroom cameras. This makes the stereo rectification problem more challenging for satellite images.

For rectifying full chips we take piecewise homographies and stitch them together. Subsequently, we compute x - and y -maps that can transform a grid in the stereo rectified coordinate space to the unrectified image coordinate space. Since unrectified chip pairs are broken into non-overlapping tiles, simply stitching the corresponding rectified tiles can result in missing image information near the edges. In order to get smoother boundaries, we use overlapping tiles and average the x - and y - coordinates in the overlapping regions in the rectified space. We generate both rectification and inverse rectification maps in this step, in order to go back and forth between an unrectified view and the corresponding stereo rectified view.

4.5. Generating a Chip-Level Fused DSM

We now briefly describe our procedure to obtain chip-level pairwise DSMs and a fused DSM for each AOI.

Using water masks from SRTM DEM, the water regions in the individual tiles are masked out and such points are marked invalid in the output DSM. As explained in Section 4.4.1 each tile pair is stereo rectified and then we use SGM [16] for stereo matching. Then using the estimated tile-level disparity maps we perform triangulation to get a point cloud per tile. All the pairwise tile-level pointclouds are merged to form a pairwise chip-level pointcloud which is converted into a pairwise chip-level DSM.

After obtaining a sufficient number of pairwise chip-level DSMs, we fuse these by taking the median over all valid height values at each point in the output grid. We then use the alignment tool provided by [1] for estimating the required translation to align LiDAR to the fused DSM.

5. Generating the Disparity Groundtruth from LiDAR

Figure 5 shows the overview of our process for generating groundtruth disparity maps. We first take all the points from a stereo rectified reference view and map into the corresponding unrectified reference view. This is shown as the arrow with Label 1 in Figure 5. Then we backproject these point coordinates, onto LiDAR, using the corresponding RPC model. Note that the backprojected ray may intersect the LiDAR at multiple points, so we ensure that the system returns the point that is actually visible from the satellite, i.e. the point with the greatest height. We use bilinear interpolation for missing points in LiDAR e.g. building walls. This step returns a world point (latitude, longitude and height) for each backprojected image point. This step is marked by the arrow with Label 2 in Figure 5. In step 3 we take all these world points and project them onto the unrectified secondary view using its RPC model. In the last step 4, we map these point into the secondary rectified view. After these steps 1 through 4 we get correspondences in two stereo rectified views, as shown by labeled points \mathbf{p} and \mathbf{q} in Figure 5. Then we can use the definition of disparity to compute a reference disparity map \mathbf{D}_b . As shown in Figure 5, disparity at point \mathbf{p} can be calculated as

$$\mathbf{D}_{b\mathbf{p}} = \mathbf{q}_x - \mathbf{p}_x$$

We repeat the same process by switching the order of the two views to get the corresponding secondary disparity map \mathbf{D}_m . Then we perform a consistency check in the form of the Left-Right-Right-Left (LRRLL) check to detect and mark occluded pixels as invalid, which is given as

$$\mathbf{D}_{b\mathbf{p}} = \begin{cases} \mathbf{D}_{b\mathbf{p}} & \text{if } |\mathbf{D}_{b\mathbf{p}} - \mathbf{D}_{m\mathbf{s}}| \leq 1 \\ \text{invalid} & \text{otherwise} \end{cases} \quad (1)$$

where $\mathbf{s} = [\mathbf{p}_x + \mathbf{D}_{b\mathbf{p}}, \mathbf{p}_y]^T$

5.1. Creating Building Masks

For generating building masks for the rectified chips, we obtain an initial building mask in lat/long space by applying the tool from [1] on the aligned LiDAR. However, we noticed that occasionally, some trees or vegetation do get marked as buildings. Therefore, we manually clean up the initial masks. Then we project the points corresponding to buildings onto unrectified chips. Finally using the inverse rectification maps, we map these masks into the rectified chips.

6. Results

This section is organized as follows. We first present a quantitative evaluation of our rectification errors in Section 6.1 and in the following section 6.2 we present a quantitative evaluation of our groundtruth disparity maps using human annotated tie points. Figure 1 shows some example images and groundtruth disparity maps from the top four largest AOIs, along with building masks and metadata.

6.1. Rectification Errors

Since one of the major challenges with using pushbroom camera models is stereo rectifying the full chips, we present an evaluation of our stereo rectification method here. Figure 6 shows the distribution of average y-errors across all the pairs in each dataset. For calculating these errors, we project world points sampled from a 3D grid onto the unrectified views and then using inverse rectification maps, we map them into the rectified views. We then calculate the absolute y-error for each point and then compute the average. We use around 4000 world points. Across all the pairs in each dataset, our average rectification errors remain within half a pixel. As can be seen by the mean values that are displayed separately for each histogram in Figure 6, these errors are comparable to those for the Middlebury2014 dataset [24], for which the reported average error is 0.2 pixels.

6.2. Quantitative Evaluation

In this Section we present a quantitative evaluation of the disparity maps for the two largest AOIs - UCSD and Jacksonville. We have collected some human annotated tie points in some views and we use them to quantitatively evaluate the errors in our groundtruthed disparity maps. Figure 7 shows disparity error distribution over all the groundtruth disparity pairs of UCSD WV3 and Jacksonville datasets. The average disparity error in UCSD is 1.23 pixels and for Jacksonville it is 1.84 pixels. These errors are obviously not sub-pixel — possibly on account of the fact that the LiDAR values are only known with 30 cm resolution.

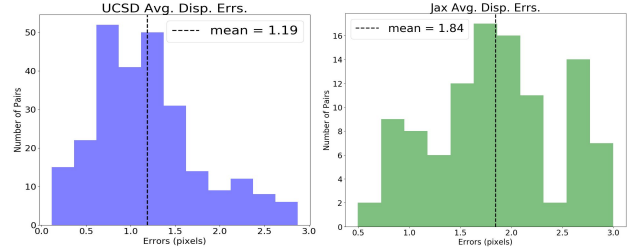


Figure 7: Disparity errors (using human annotated ground truth points) distribution for UCSD WV3 and Jacksonville AOIs

6.3. Stereo Matching Experiment

In this section we show stereo matching results to illustrate the challenges posed by out-of-date stereo pairs. Using the groundtruthed disparities in our datasets, Figure 8 shows the percentage of pixels where the errors exceed one pixel in the estimated disparities using the SGM [16] and MSMW [9] algorithms. We also show two cases with regard to the interval between the image acquisition times. In one case the time interval is less than one month and in the other case it is between 100 days and 250 days. We use the building masks to evaluate the errors.

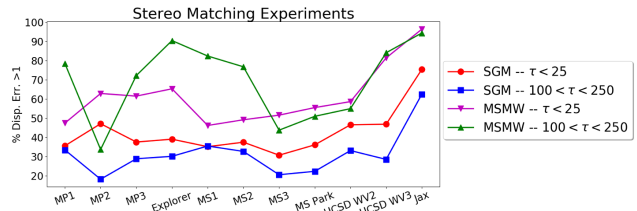


Figure 8: Stereo Matching results – “ $\tau < 25$ ” denotes results on pairs where the time interval is less than a month and “ $100 < \tau < 150$ ” denotes results on pairs where the interval is between 100 to 250 days.

7. Conclusion

We have contributed a large benchmarking stereo dataset for out-of-date satellite images and also provided a framework for how such a dataset can be constructed. In the dataset we make available, the rectification accuracy is comparable to the existing state-of-the-art datasets. Unlike the existing benchmarking datasets, we have also carried out a quantitative evaluation of our groundtruthed disparities using human annotated points in two AOIs. Our stereo matching experiments show that this dataset presents a new level of challenge for stereo matching algorithms, both in terms of stereo-pair sizes and scene variations. We hope that re-

searchers in the stereo reconstruction and remote sensing areas will benefit from this dataset.

8. Acknowledgements

Supported by the Intelligence Advanced Research Projects Activity (IARPA) via Department of Interior / Interior Business Center (DOI/IBC) contract number D17PC00280. The U.S. Government is authorized to reproduce and distribute reprints for Governmental purposes notwithstanding any copyright annotation thereon. Disclaimer: The views and conclusions contained herein are those of the authors and should not be interpreted as necessarily representing the official policies or endorsements, either expressed or implied, of IARPA, DOI/IBC, or the U.S. Government.

References

- [1] Open source geospatial tools for 3d registration and scene classification. <https://www.jhuapl.edu/pubgeo/170807-FOSS4G-JHUAPL-Open-Source-Geospatial-Tools.pdf>. 7, 8
- [2] Radiometric use of worldview-2 imagery. https://dg-cms-uploads-production.s3.amazonaws.com/uploads/document/file/104/Radiometric_Use_of_WorldView-2_Imagery.pdf. 5
- [3] Radiometric use of worldview-3 imagery. https://dg-cms-uploads-production.s3.amazonaws.com/uploads/document/file/207/Radiometric_Use_of_WorldView-3_v2.pdf. 5
- [4] Bundle Adjustment-A Modern Synthesis. *Vision Algorithms*, 34099:298–372, 2000. 5
- [5] SURF: Speeded up robust features. volume 3951 LNCS, pages 404–417, 2006. 5
- [6] M. Bosch, K. Foster, G. Christie, S. Wang, G. D. Hager, and M. Brown. Semantic stereo for incidental satellite images. In *2019 IEEE Winter Conference on Applications of Computer Vision (WACV)*, pages 1524–1532, Jan 2019. 4
- [7] M. Bosch, Z. Kurtz, S. Hagstrom, and M. Brown. A multiple view stereo benchmark for satellite imagery. In *2016 IEEE Applied Imagery Pattern Recognition Workshop (AIPR)*, pages 1–9. IEEE, 2016. 1
- [8] M. Brown, H. Goldberg, K. Foster, A. Leichtman, S. Wang, S. Hagstrom, M. Bosch, and S. Almes. Large-scale public lidar and satellite image data set for urban semantic labeling. In *Laser Radar Technology and Applications XXIII*, volume 10636, page 106360P. International Society for Optics and Photonics, 2018. 1
- [9] A. Buades and G. Facciolo. Reliable multiscale and multiwindow stereo matching. *SIAM Journal on Imaging Sciences*, 8(2):888–915, 2015. 8
- [10] D. J. Butler, J. Wulff, G. B. Stanley, and M. J. Black. A naturalistic open source movie for optical flow evaluation. In A. Fitzgibbon et al. (Eds.), editor, *European Conf. on Computer Vision (ECCV)*, Part IV, LNCS 7577, pages 611–625. Springer-Verlag, Oct. 2012. 3
- [11] C. De Franchis, E. Meinhardt-Llopis, J. Michel, J.-M. Morel, and G. Facciolo. An automatic and modular stereo pipeline for pushbroom images. In *ISPRS Annals of the Photogrammetry, Remote Sensing and Spatial Information Sciences*, 2014. 4, 5
- [12] G. Facciolo, C. De Franchis, and E. Meinhardt-Llopis. Automatic 3d reconstruction from multi-date satellite images. In *Proceedings of the IEEE Conference on Computer Vision and Pattern Recognition Workshops*, pages 57–66, 2017. 5
- [13] A. Geiger, P. Lenz, and R. Urtasun. Are we ready for autonomous driving? the kitti vision benchmark suite. In *Conference on Computer Vision and Pattern Recognition (CVPR)*, 2012. 3
- [14] J. Grodecki and G. Dial. Block adjustment of high-resolution satellite images described by Rational Polynomials. *Photogrammetric Engineering and Remote Sensing*, 69(1):59–68, 2003. 5
- [15] R. Hartley and A. Zisserman. *Multiple view geometry in computer vision*. Cambridge university press, 2003. 5
- [16] H. Hirschmuller. Stereo processing by semiglobal matching and mutual information. *IEEE Transactions on pattern analysis and machine intelligence*, 30(2):328–341, 2008. 7, 8
- [17] H. Hirschmuller and D. Scharstein. Evaluation of cost functions for stereo matching. In *2007 IEEE Conference on Computer Vision and Pattern Recognition*, pages 1–8. IEEE, 2007. 3
- [18] C. Loop and Z. Zhang. Computing rectifying homographies for stereo vision. In *Proceedings. 1999 IEEE Computer Society Conference on Computer Vision and Pattern Recognition (Cat. No PR00149)*, volume 1, pages 125–131. IEEE, 1999. 5
- [19] D. G. Lowe. Distinctive image features from scale-invariant keypoints. *International journal of computer vision*, 60(2):91–110, 2004. 5
- [20] M. Menze and A. Geiger. Object scene flow for autonomous vehicles. In *Conference on Computer Vision and Pattern Recognition (CVPR)*, 2015. 3
- [21] Y. Nakamura, T. Matsuura, K. Satoh, and Y. Ohta. Occlusion detectable stereo-occlusion patterns in camera matrix. In *Proceedings CVPR IEEE Computer Society Conference on Computer Vision and Pattern Recognition*, pages 371–378. IEEE, 1996. 3
- [22] J. Oh, W. H. Lee, C. K. Toth, D. A. Grejner-Brzezinska, and C. Lee. A piecewise approach to epipolar resampling of pushbroom satellite images based on rpc. *Photogrammetric Engineering & Remote Sensing*, 76(12):1353–1363, 2010. 4
- [23] I. R. Otero. *Anatomy of the SIFT Method*. PhD thesis, École normale supérieure de Cachan-ENS Cachan, 2015. 5
- [24] D. Scharstein, H. Hirschmüller, Y. Kitajima, G. Krathwohl, N. Nešić, X. Wang, and P. Westling. High-resolution stereo datasets with subpixel-accurate ground truth. In *German conference on pattern recognition*, pages 31–42. Springer, 2014. 3, 8
- [25] D. Scharstein and R. Szeliski. A taxonomy and evaluation of dense two-frame stereo correspondence algorithms. *International journal of computer vision*, 47(1-3):7–42, 2002. 3

- [26] D. Scharstein and R. Szeliski. High-accuracy stereo depth maps using structured light. In *2003 IEEE Computer Society Conference on Computer Vision and Pattern Recognition, 2003. Proceedings.*, volume 1, pages I–I. IEEE, 2003. 3
- [27] T. Schops, J. L. Schonberger, S. Galliani, T. Sattler, K. Schindler, M. Pollefeys, and A. Geiger. A multi-view stereo benchmark with high-resolution images and multi-camera videos. In *Proceedings of the IEEE Conference on Computer Vision and Pattern Recognition*, pages 3260–3269, 2017. 3